Fracture properties and microstructure formation of hardened alkali-activated slag/fly ash pastes

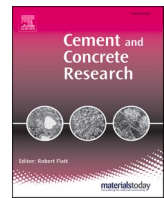Zhang, Shizhe; Li, Zhenming; Ghiassi, Bahman; Yin, Suhong; Ye, Guang

Important note
To cite this publication, please use the final published version (if applicable).
Please check the document version above.

Fracture properties and microstructure formation of hardened alkali-activated slag/fly ash pastes

Shizhe Zhang [a],[*], Zhenming Li [a], Bahman Ghiassi [a],[b], Suhong Yin [c], Guang Ye [a],[c],[*]

[a] *Microlab, Section Materials and Environment, Faculty of Civil Engineering and Geosciences, Delft University of Technology, Stevinweg 1, 2628 CN, Delft, the Netherlands*
[b] *Centre for Structural Engineering and Informatics, Faculty of Engineering, University of Nottingham, Nottingham, United Kingdom*
[c] *School of Materials Science and Engineering, South China University of Technology, Guangzhou, China*

A B S T R A C T

This study presents a comprehensive experimental investigation on the fracture properties of hardened alkali-activated slag/fly ash (AASF) pastes in relation to the microstructure formation and reaction product composition. The main reaction product in AASF is C-(N-)A-S-H gel along with minor hydrotalcite phase, with the polymerization of C-(N-)A-S-H gel substantially governed by its Ca/Si ratio. Strong positive correlations are identified between the Ca/Si ratios of C-(N-)A-S-H gel and the fracture properties K_{Ic} (J_{tip}), whereas, the compressive strength of AASF pastes is primarily determined by its capillary porosity (>0.01 μm). The disagreements between the Ca/Si ratios and corresponding intrinsic mechanical properties of C-(N-)A-S-H gel as proof by contradiction indicate that the fracture properties K_{Ic} (J_{tip}) of AASF pastes could be dominated by a cohesion/adhesion-based mechanism. These findings provide promising guidance for fine-tuning the fracture properties of AASF and also advise on the tailoring strategies for high-performance composite such as strain-hardening geopolymer composite.

1. Introduction

The recent technical development concerning a circular economy for mineral waste materials within the Netherlands and the European Union (EU) has been proved to be highly sustainable and economically profitable. Within construction sectors, alkali-activation technology has emerged as an effective tool to reuse different mineral wastes and industrial by-products to produce cement-free building materials. Compared with traditional cementitious materials, alkali-activated materials (AAMs) or geopolymers derived by the reaction of an alkali metal source (solid or dissolved) with a solid aluminosilicate powder [1] are environmental-friendly and need only moderate energy to produce [2]. As one of the promising alternatives for ordinary Portland cement (OPC), AAMs maintain comparable and even better performance to traditional cementitious binders. It has been reported that these materials can have superior mechanical properties and durability when compared with several types of existing OPC-based concrete under current standards. Furthermore, they also can provide added advantage to greenhouse gas emission reduction with up to 80% compared to OPC [3]. Among all AAMs, the ones based on blast furnace slag, class F fly

ash, and their blends are most intensively studied due to the large quantity of annual production as well as the relatively stable chemical compositions of these two solid precursors [1,3]. Previous studies on alkali-activated slag/fly ash (AASF), have focused on its microstructure development, nature of reaction products as well as mechanical properties [4–7]. AASF as a binder has been already applied in many engineering practices. Certain concerns have been raised by researchers stating that the production of AASF binder creates resource competition with the blended cementitious materials. However, this situation can be solved by using other abundant industrial by-products as solid precursors with further research and development [8].

For the application of AASF as an intrinsically brittle material, the challenges come not only from the strength development but also from its fracture properties. For the structural application of AASF, the fracture properties, which reflect the material resistance to fracture initiation and propagation, play equally important or sometimes even more important roles as strength development. However, studies on the fracture properties of AASF, which are essential for engineering design and safety assessment of AASF-based concrete as construction materials, are still quite limited when compared with those on traditional

* Corresponding authors
E-mail addresses: Shizhe.Zhang@tudelft.nl (S. Zhang), G.Ye@tudelft.nl (G. Ye).

cementitious systems. To the best of the authors' knowledge, only very few have reported the fracture properties of AAMs. Nath and Sarker studied the ambient temperature cured AASF-based concrete and found that it was comparable with their OPC concrete regarding their load-deflection behavior. Besides, the fracture toughness (K_{Ic}), which is comparable to that of OPC concrete under similar compressive strength, shares a similar trend with the flexural strength. The fracture energy (G_F), on the other hand, agrees well with the trend of compressive strength [9]. Ding et al. reported the fracture properties of ambient temperature cured AASF-based concrete. They found that the Bazant and Becq-Giraudon model better predicts the fracture energy of AASF-based concrete as a function of compressive strength over the CEB/FIP model proposed jointly by the Euro-International Committee for Concrete (CEB) and the International Federation for Prestressing (FIP). Furthermore, their study confirmed fracture behavior of AASF-based concrete is affected by different materials parameters, including alkali concentration, silicate modulus of alkaline activator, slag/fly ash ratios as well as liquid to binder ratio [10]. Other works concerning fracture properties of AAMs relate to heat-cured fly ash-based alkali-activated concrete. Pan et al. measured the fracture properties of fly ash-based geopolymer paste and concrete. Except for the lower characteristic lengths and higher brittleness compared to OPC concrete counterpart, the fracture properties were found to be closely related to the compressive strength of the mixtures [11]. Another set of studies concerning fracture properties of AAMs including the AASF system are associated with the development of strain-hardening geopolymer composite (SHGC). Due to the significance of matrix K_{Ic} as a substantial influencing parameter on the crack propagation, crack-bridging, and consequently the strain-hardening and multiple cracking behaviors of SHGC [12,13]. However, all these studies limit themselves to the experimental testing of K_{Ic} to reflect the crack propagation resistance of the matrix [13–15].

Up till now, not only the amount of existing studies concerning fracture properties of AASF is limited, the study on fracture-related microstructural aspects is also largely omitted. Since the fracture resistance relates intimately to material microstructure [16], comprehensive microstructure studies seem inevitable towards a sound design or tailoring strategies for the toughening of AASF. Therefore, this study aims to experimentally investigate the fracture properties of hardened AASF paste combined with microstructure characterization to provide a better understanding of the fracture in AASF. The fracture toughness (K_{Ic}), crack-tip toughness (J_{tip}), and fracture energy (G_F) were studied using three-point bending tests (Section 3.2). Other mechanical properties including compressive strength and elastic modulus of the hardened AASF paste were tested as well (Section 3.1). The microstructural formation was characterized using multiple techniques with regards to the chemical composition, pore structure, and amount of reaction product formation in hardened AASF paste (Section 3.3). The microstructural aspects are further correlated with the tested fracture properties and mechanical properties (Section 3.4). Based on this, the fracture mechanism of hardened AASF paste is extrapolated and discussed (Section 3.4), which advises on the strategies for future design and tailoring of its fracture properties.

2. Experimental program

2.1. Materials

The solid precursors used in this study were ground granulated blast furnace slag and Class F fly ash according to ASTM 618 [17] produced locally in the Netherlands. The material density of slag and fly ash are 2890 kg/m^3 and 2440 kg/m^3, respectively. The d_{50} particle size is 17.88 μm for slag and 33.19 μm for fly ash. The chemical compositions determined by X-ray Fluorescence along with the loss on ignition (LOI) at 950 °C, and fineness passing 45 μm are shown in Table 1. As has been reported in our previous studies [14,18], the main crystalline phases determined by powder X-ray diffraction (XRD) in fly ash are quartz, mullite, and hematite, while the blast furnace slag contains mainly amorphous phases. The reactivity of fly ash is reflected by its reactive silica content (43.04%) and reactive alumina content (14.51%) as determined by selective chemical dissolution [18]. The slag, on the other hand, has mainly amorphous phases (>95%) [19]. The high reactivity slag in the alkaline environment has been confirmed previously using isothermal calorimetry [18].

The alkaline activator was prepared using sodium hydroxide pellets (analytical grade, purity ≥98%), liquid sodium silicate solution (Na_2O: 8.25 wt%, SiO_2: 27.50 wt%, and H_2O: 64.25 wt%), and distilled water to achieve different silicate modulus (M_s). The activator was cooled down to room temperature (20 °C) prior to mixture preparation.

2.2. Mixture design and preparation

The mixture design originates from an AASF paste that exhibits a good combination of mechanical properties, workability, and setting time [20]. It has been reported that the microstructure and reaction kinetics of AASF is significantly influenced by the contents of available Ca and Si [4,18,21]. Thus, both the slag/fly ash content and the silicate modulus M_s (M_s being the SiO_2/Na_2O molar ratios) of the activator play important roles in determining the mechanical properties of the mixture [22,23]. Accordingly, the slag content and the M_s of the alkaline activator were selected as the main variables in this study. The detailed mixture designs are shown in Table 2, in which two types of binder composition with different slag content (S30 and S50) and activator with different M_s (0–1.5) were given. In each of the mixture, the w/b ratio and Na_2O content (in activator with respect to total binder mass) were kept constant to be 0.32 and 4.0 wt%, respectively. The w/b ratio was chosen in a way that adequate workability for all paste mixtures was maintained. The mixtures were categorized into two systems: sodium

Table 2
Mixture proportions of alkali-activated slag/fly ash pastes.

Mixture[a]	Precursor		Alkaline activator (wt%)			
	Slag (wt %)	Fly ash (wt%)	Water	Na_2O	SiO_2	Silicate modulus (M_s)
S30M0	30	70	32	4.0	0	0
S30M0.5					1.94	0.50
S30M0.8					3.10	0.80
S30M1.0					3.88	1.00
S30M1.2					4.65	1.20
S30M1.5					5.82	1.50
S50M0	50	50	32	4.0	0	0
S50M0.5					1.94	0.50
S50M0.8					3.10	0.80
S50M1.0					3.88	1.00
S50M1.2					4.65	1.20
S50M1.5					5.82	1.50

[a] Mixture notations: S indicates the weight percentage of slag in the slag/fly ash binder. M indicates the silicate modulus M_s of the alkaline activator used for mixture preparation.

Table 1
Chemical compositions and properties of raw materials.

Oxide (wt%)	SiO_2	Al_2O_3	Fe_2O_3	CaO	MgO	SO_3	Na_2O	K_2O	LOI	Fineness, % passing 45 μm
Slag	32.91	11.84	0.46	40.96	9.23	1.60	–	0.33	1.15	95
Fly ash	52.90	26.96	6.60	4.36	1.50	0.73	0.17	–	3.37	81

hydroxide-activated system (with no soluble silicate in the activator) and sodium silicate-activated system (with soluble silicate in the activator).

The solid precursors were firstly dry mixed for 5 min using a HOBART® mixer at a low speed. Alkaline activator solution was then gradually added and the batches were mixed for an additional 5 min at a medium speed (285 rpm). The fresh paste mixtures were cast in polystyrene prism molds (40 mm × 40 mm × 160 mm) and then compacted on a vibration table before finally sealed with a plastic wrap. The samples were demolded after 1 day and were cured in a climate room (20 °C and ≥98% RH) before testing.

the notch on the side surfaces of the prism. The prism was supported over a load span (S) of 120 mm. The detailed testing set-up is shown in Fig. 1. At least 6 tests were conducted on each mixture.

Assuming that linear elastic fracture mechanics (LEFM) holds for the AASF paste as a fine grain matrix material, the fracture toughness K_{Ic}, i. e. mode I critical stress intensity factor, is computed from Eq. (1) using the peak load P_{Max} [N] from the 3PB test while considering the specimen-related shape function, as has been widely used in previous studies and recommendations [11,13,14,27,28].

$$K_{Ic} = \frac{1.5 \, P_{Max} \, S \, \sqrt{\pi a}}{B \, W^2} \left(\frac{0.68 - 0.744\alpha}{1 - 2.155\alpha + 1.161\alpha^2} + 0.36 - 2.088\alpha + 4.611\alpha^2 - 6.499\alpha^3 + 4.232\alpha^4 \right) \qquad (1)$$

2.3. Testing procedures

2.3.1. Compressive strength and elastic modulus tests

The compressive strength of AASF specimens cured for 28 days was measured according to EN 196-1 standard [24]. The 28-day elastic modulus was obtained using 40 × 40 × 160 mm^3 prismatic specimens following a modified set-up according to ASTM C496 [25]. The tests were conducted on a close-loop INSTRON machine using load-control with a rate of 0.1 MPa/s, which consists of four loading-unloading cycles with the stress ranges from 5% to 15% of the compressive strength. The strain was measured simultaneously using four linear variable differential transformers (LVDTs) attached on each side of the prism. At least three specimens for each mixture were tested for reproducibility and the loading elastic modulus was calculated using the last three stress-strain curves of the loading process. It is crucial to note here that the loading elastic modulus could to some extent deviates from the true elastic modulus due to the viscoelasticity of the material [26]. However, considering that the quasi-static loading regime of the tests and the 28 days' curing age of the pastes, the tested loading modulus is considered as the suitable estimate of the elastic moduli of AASF pastes.

2.3.2. Three-point bending tests on single-edge notched beam

The fracture toughness K_{Ic} of AASF paste was determined using single-edge notched specimens with 40 mm in depth (W), 40 mm in width (B), and 160 mm in length. The single-edge notches with 1.5 mm in width, 40 mm in length, and 12 mm in notch depth (a) were prepared using a diamond cutting saw prior to testing. The relative notch depth ratio α (α = a/W) was kept to be 0.3. The three-point bending (3PB) tests were performed on a closed-loop INSTRON machine with the crack mouth opening displacement (CMOD) rate of 0.01 mm/min. The CMOD was controlled using two LVDTs, which were attached to the two sides of
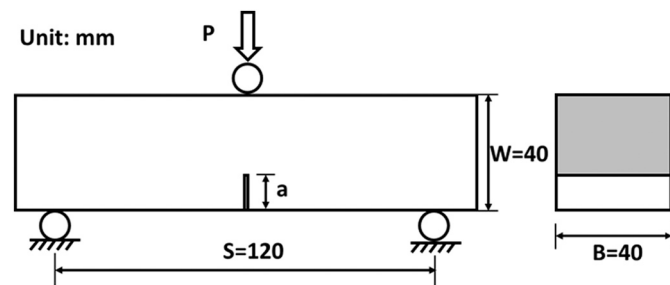
where P_{Max} is the highest applied load [N], B is the specimen width [mm], W is the specimen depth [mm], S is the loading span [mm], a is the notch depth and α = a/W (0.05 ≤ α ≤ 0.8) is the relative notch depth ratio.

Additionally, crack tip toughness J_{tip}, i.e. the critical strain energy release rate, is calculated to provide insights from an energy perspective:

$$J_{tip} = \frac{K_{Ic}^2}{E_m} \qquad (2)$$

where E_m is the elastic modulus of the paste [GPa]. As discussed in Section 2.3.1, using the loading elastic modulus does not introduce a significant viscoelastic part into E_m. Eq. (2) to calculate J_{tip} as one property of the materials under LEFM thereby remains valid.

Work-of-fracture based fracture energy G_F is calculated according to RILEM recommendation by TC-FMC:

$$G_F = \frac{W_0 + mg \, \delta_0}{A_{lig}} = \frac{\int_0^{\delta_0} P(\delta) \, d\delta + mg \, \delta_0}{W \, (B - a)} \qquad (3)$$

where W_0 is the area under the load-CMOD curve [J], m is the mass of the beam between support [kg], g is gravity constant [m/s^2], δ_0 is the final mid-point deflection [μm] and Al_{ig} is the ligament area calculated by specimen dimensions [m^2]. It is worth noting that W_0 in this study is calculated using CMOD instead of mid-point deflection δ_0 following [29]. This calculation is based on the linear relationship that exists between CMOD and mid-point deflection in 3PB tests on single-edge notched prism samples, which has been experimentally confirmed by previous research [30–32]. G_F calculated using CMOD is in general smaller than G_F calculated using δ_0 and the magnitude of G_F reduction is related to the sample geometry.

2.3.3. Microstructural characterization

All microstructural characterization tests were performed on AASF paste samples cured for 28 days. Previous to testing, the investigated samples were crushed into small pieces and their reaction was stopped by solvent exchange using isopropanol followed by vacuum drying.

The chemical compositions of reaction products were characterized by environmental scanning electron microscopy (ESEM) and energy dispersive X-ray (EDX) analysis, using a Philips-XL30-ESEM equipped with a Thermofisher UltraDry EDX detector. After the reaction stoppage, the samples were impregnated using low viscosity epoxy resin and polished down to 0.25 μm using ethanol [33]. The polished samples were then coated with carbon and the EDX measurement was conducted at an accelerating voltage of 15 kV in high vacuum mode. It should be noted that the atomic number, absorption, and fluorescence (ZAF) corrections were made in each EDX measurement, which is an implemented function in the Pathfinder software. ZAF corrections could convert apparent concentrations (raw intensities) into corrected concentrations

Fig. 1. Three-point bending test configuration for single-edge notched prism specimen [14].

to eliminate inter-element matrix effects, which makes it possible for semi-quantitative comparisons of element ratios.

Thermogravimetry and differential thermogravimetry (DTG) was performed in a TG-449-F3-Jupiter instrument for analysis of the reaction products. The powder of samples was put in a small aluminum oxide crucible and heated from 40 °C to 1100 °C at 10 °C/min in an argon protection atmosphere at a flow speed of 50 μL/min.

The chemical bonds formed within the reaction products were determined by Attenuated total reflection-Fourier-transform infrared spectroscopy (ATR-FTIR) using a Spectrum TM 100 Optical ATR-FTIR spectrometer over the wavelength range of 600 to 4000 cm^{-1} with a resolution of 1 cm^{-1}.

The pore structures were measured by nitrogen gas adsorption using a Gemini VII 2390 instrument. The relative pressure defined as the equilibrium vapor pressure divided by the saturation vapor pressure (p/p$_0$) ranges from 0.05 to 0.99, which corresponds to a pore size from 0.002 to 0.1 μm. The pore size distribution is derived using Barrett-Joyner-Halenda models.

3. Results and discussions

3.1. Compressive strength and elastic modulus

The compressive strength and the elastic modulus of AASF paste at 28 days are plotted as a function of M$_s$ ranging from 0 to 1.5, as shown in Fig. 2(a) and (b), respectively.

Regardless of the alkaline activators used, increasing slag content from 30 wt% to 50 wt% yielded both higher compressive strength and elastic modulus at 28 days. Slag as an aluminosilicate precursor with a higher content of amorphous phases has higher reactivity than fly ash. The Ca content within slag also promotes early age reaction kinetics, which is beneficial for strength development [7]. Furthermore, the effect induced by activator M$_s$ on both mechanical properties is also significant. As depicted in Fig. 2, the sodium hydroxide-activated systems (M$_s$ = 0) have substantially lower compressive strength and elastic modulus when compared with sodium silicate-activated systems (M$_s$ = 0.5–1.5). The mechanical properties of both S30 and S50 change evidently, which with increasing M$_s$ first increases and then decreases after reaching a maximum. Specifically, the 28-day maximum compressive strength of S30 and S50 mixtures are 62.6 MPa and 80.3 MPa, respectively. With regards to the M$_s$ of activator, it determines the availability of soluble silica from the activator. Increasing M$_s$ could thereby alter the geopolymerization process, influence the amount of reaction product, and consequently the mechanical properties [21,34]. However, an excessive

amount of silica is not favorable as well since it can retard the dissolution of slag as well as the further polycondensation reaction, which may harm the strength development [21,34,35]. Therefore, optimum activation conditions for AASF could only be achieved using moderate M$_s$. Either too low or too high M$_s$ is not favored for the compressive strength development.

Furthermore, the discrepancies between the compressive strength and elastic modulus development with increasing M$_s$ could be observed. The compressive strength peaked at a M$_s$ of 1.0 while the elastic modulus at M$_s$ of 0.5. The AASF paste as a heterogeneous porous material is believed to behave similarly to cement paste. Since the pores within AASF paste serve as the weakest links within the materials, the compressive strength is governed by porosity [36]. On the other hand, the elastic modulus is not dependent on the porosity alone but also on the elastic moduli of other reaction products [37]. Consequently, it is not surprising that the maximum compressive strength and elastic modulus were achieved at slightly different M$_s$.

3.2. Fracture properties

The fracture properties of AASF pastes including K$_{Ic}$ (J$_{tip}$), and G$_F$ derived from 3PB tests on single-edge notched prismatic specimens are discussed in this section. The representative load vs CMOD curves of each AASF paste are illustrated in Fig. 3(a) and (b). The load-CMOD curves of AASF paste share similar characteristics as that of cementitious materials and consist of a linear elastic part followed by an elastic-plastic stage before reaching the peak load P$_{max}$. After reaching P$_{max}$, the paste went through a strain-softening behavior as the crack continuously propagated. This characteristic relates closely to the brittleness of the mixture. It should be noted that the post-peak softening branch of S50M0 and S50M0.5 mixtures could not be obtained by controlling CMOD, which is possibly due to the higher inherent brittleness than other mixtures. It could be observed that AASF mixtures with various slag content and M$_s$ show different fracture properties with different magnitudes of P$_{max}$ as well as the post-peak behaviors.

3.2.1. Fracture toughness and crack tip toughness

The fracture toughness K$_{Ic}$ generally increases with M$_s$ from 0 to 0.5 and then gradually decreases with increasing M$_s$ as shown in Fig. 4(a). Similar to compressive strength results, S50 mixtures have higher K$_{Ic}$ than S30 mixtures. Except for S50M0 and S50M0.5 mixtures, the K$_{Ic}$ of AASF paste in general falls in the range of 0.13 to 0.36 MPa·m$^{1/2}$, which is comparable to the K$_{Ic}$ of OPC paste (0.2 to 0.6 MPa·m$^{1/2}$) [28,38,39] as well as K$_{Ic}$ of AASF reported by Nematollahi et al. [15], and fly ash-
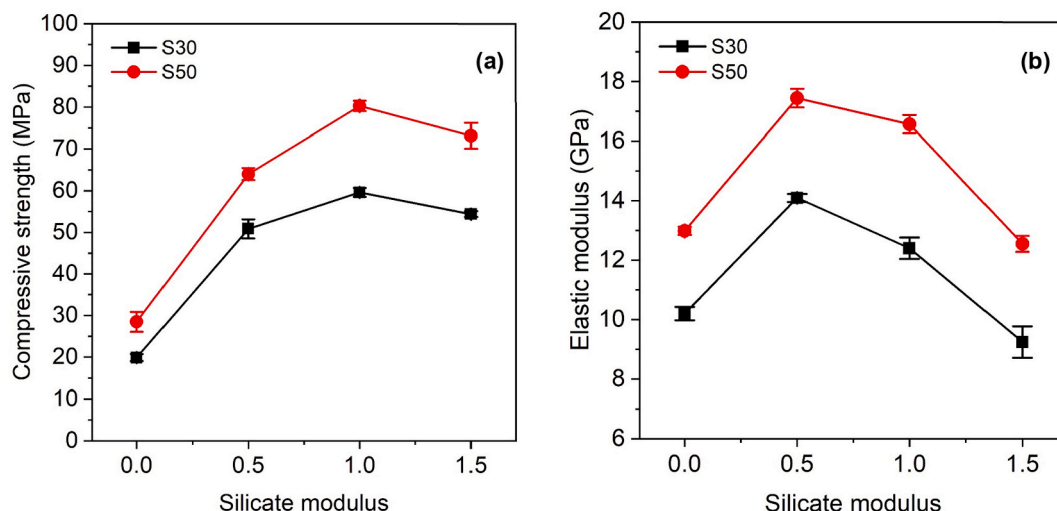

Fig. 2. (a) Compressive strength and (b) elastic modulus of AASF pastes as a function of activator silicate modulus 0, 0.5, 1.0, and 1.5.
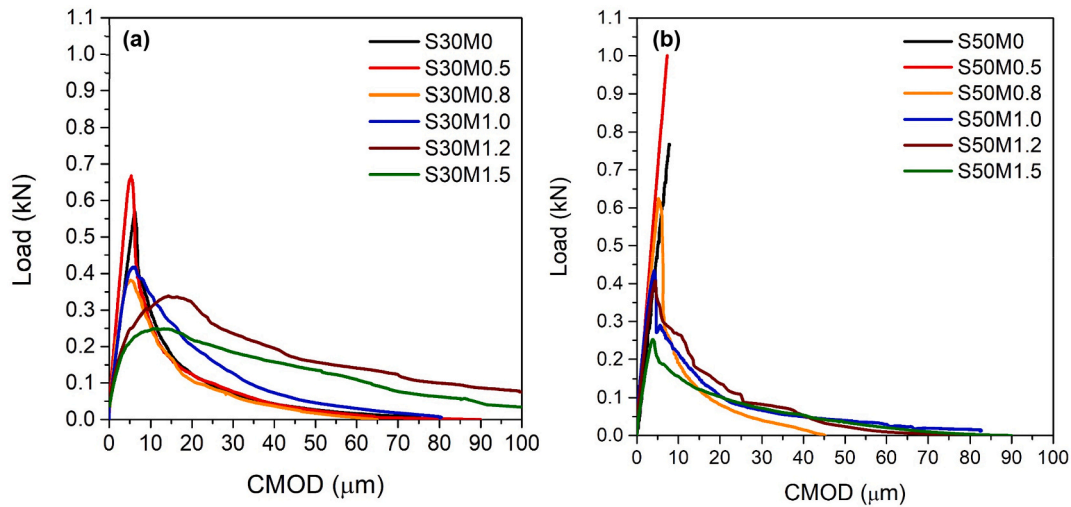
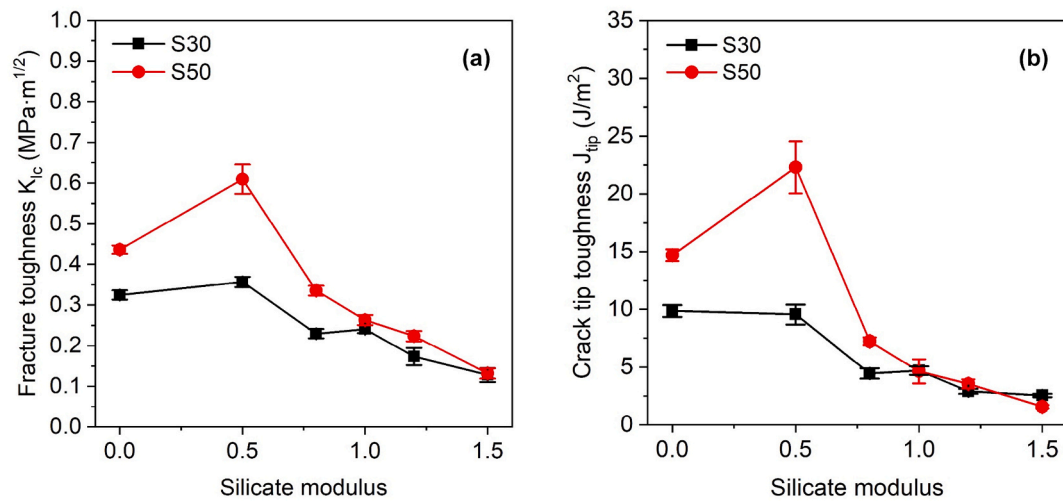**Fig. 3.** Representative Load-CMOD curves for AASF pastes (a) S30 and (b) S50 series.

Fig. 4. (a) Fracture toughness K_{Ic} and (b) crack tip toughness J_{tip} of AASF pastes as a function of activator silicate modulus 0, 0.5 1.0, and 1.5.

based geopolymers paste reported by Pan et al. [11] and Ohno et al. [11,13]. The highest values of K_{Ic} are observed at the M_s of 0.5, which reaches 0.36 MPa·m$^{1/2}$ and 0.61 MPa·m$^{1/2}$ for S30 and S50 mixtures, respectively. On the other hand, crack tip toughness J_{tip} as shown in Fig. 4(b) reveals a trend that is well consistent with K_{Ic}, which reflects the effectiveness as well as the soundness of using 3PB for fracture testing of AASF paste. As in LEFM, K_{Ic} and J_{tip} (or the strain energy release rate) are uniquely related, the similar trend of J_{tip} and K_{Ic} with increasing M_s proves that the assumption of using LEFM to determine the fracture properties of AASF paste is also reasonable as for cementitious paste.

Finally, the influence of M_s on both K_{Ic} and J_{tip} of AASF follows a different trend compared to that of compressive strength. This inconsistency with the compressive strength seems somewhat counter-intuitive, however, it implies that these two properties are determined by different factors, which could not be modified simultaneously and monotonically by changing M_s only. Previous studies reported that the K_{Ic} is mainly affected by the size, texture, and angularity of aggregates as well as the microstructure of the paste [11]. A strong correlation was also found between K_{Ic} and the fracture surface roughness (R_{fs}) [40], which is one characteristic determined by the chemical composition of the reaction products in cement paste [41]. Considering the identical solid precursor combination within S30 and S50 mixtures, it can be
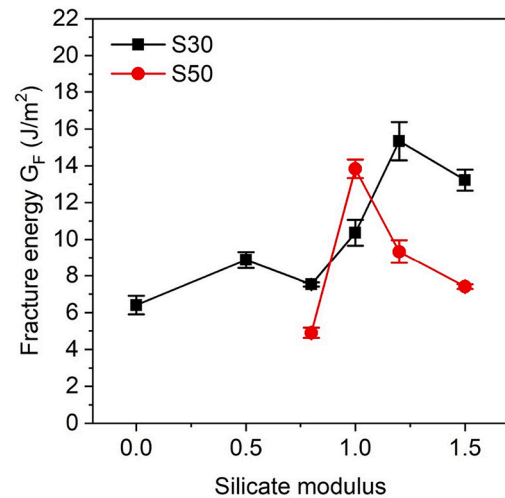

Fig. 5. Work-of-fracture based G_F of AASF pastes as a function of activator silicate modulus 0 to 1.5.

thereby inferred that the most prominent reason for the difference in K_{Ic}

of AASF lies in their different microstructures and possibly chemical composition of the reaction products. Such assumptions are further discussed with evidence from microstructure characterization in this study (Section 3.4).

3.2.2. Work-of-fracture based fracture energy

The work-of-fracture based fracture energy G_F of all investigated AASF is shown in Fig. 5. In most cases, mixtures with less slag exhibit higher G_F. The G_F of S30 and S50 mixtures peaks at M_s of 1.2 and 1.0, respectively. The values of G_F are within the range of 6 to 15 J/m^2, which are comparable to G_F reported in AASF systems [11] and primarily lower than G_F normally found in cementitious systems (15 to 30 J/m^2) [39]. The lower value of G_F, therefore, indicates that AASF is inherently more brittle than its cementitious counterparts with similar compressive strength. For an ideal brittle material, work-of-fracture based G_F should approach J_{tip} in Fig. 4(b). However, the trend of G_F with increasing M_s deviates from that of J_{tip}. This is because G_F determined by the work-of-fracture method relies not only on the peak load but also heavily on the softening curves after the peak load, which is very sensitive to the testing configuration as well as the porosity of the specimen [36]. In fact, both G_F and compressive strength reached the maximum with M_s around 1.0, the value of which also corresponds to the lowest porosity of AASF pastes (Section 3.3.3).

Despite the inevitable influence of the porosity, it is important to note here that the work-of-fracture based G_F still serves as a valuable parameter to evaluate the brittleness of the materials. Furthermore, the discordances between G_F and K_{Ic} (J_{tip}) imply that a different underlying mechanism beyond porosity is dominating K_{Ic} (J_{tip}), which makes it crucial to study microstructural aspects of the fracture properties.

3.3. Reaction product characterization

3.3.1. ESEM/EDX analysis

EDX point analysis was carried out in both S30 and S50 series of M0-M1.5 to determine the chemical compositions of reaction products in AASF paste at 28 days. The points were selected carefully within the binder region, keeping sufficient distance from the unreacted particles [42]. The CaO-SiO$_2$-Al$_2$O$_3$ ternary diagram of S30 and S50 mixtures are plotted in Fig. 6, in which Ca, Al, and Si are normalized to 100% on an oxide basis. It can be observed that all EDX data fall well in the region related to alkali-activated slag (AAS) [23,43,44] as well as AASF systems [4–6,21,45–47] as previously reported, which suggests the formation of C-A-S-H type gel as the main reaction product. The N-A-S-H phase is somehow undetected in all systems. This evidence indicates that the main reaction product is the C-(N-)A-S-H gel, which is well in line with many previous studies on AASF [4–6,18,21,48,49]. The existence of N-

A-S-H type gel, however, could not be plausibly excluded. Considering C-(N-)A-S-H as the major reaction product, the interaction volume under an acceleration voltage of 15 kV is about 1.0 to 2.5 μm into the sample surface [50]. Consequently, it is still not possible to eliminate the possibility of gel intermixing of C-(N-)A-S-H and N-A-S-H/(N,C)-A-S-H, since the segregation of intermixed gels are rather difficult due to the currently limited resolution of EDX and the lack of high-resolution techniques [4]. However, it is believed that the amount of N-A-S-H/(N,C)-A-S-H formed in investigated AASF is insignificant in comparison to that of C-(N-)A-S-H [65]. Finally, the formation of the hydrotalcite phase rich in Al and Mg is also possible considering the high Mg in slag, which was confirmed in similar AASF systems [18,19].

In this study, the phase assemblage and chemical composition of C-(N-)A-S-H gel is reflected by its Ca/Si ratio, which was estimated by performing EDX analysis on flat-polished samples [51,52]. The soundness of Ca/Si ratios from EDX data was examined and fitted using the simple Gaussian curve with the minimization of the least-squares by Origin Software. All Ca/Si ratios of investigated mixtures fitted Gaussian distribution quite well and two representative histograms of Ca/Si ratios in S30M1.2 and S50M1.2 are given in Fig. 7(a) and (b), respectively. Besides, the corresponding Ca/Si box plots are illustrated. According to the central limit theorem in statistics, a good fit with Gaussian distribution indicates that the results are affected by a large number of independent random variables, or in this case, the random error induced by the experimental equipment and procedures or due to the intermixing of multiple phases within reaction products. Consequently, the mean values (μ) of both data sets of Ca/Si ratio (S30 and S50) serves as a reasonable approximation of the main reaction product (C-(N-)A-S-H gel) chemical composition in each AASF matrix.

The box plots of Ca/Si ratios of the main reaction products (C-(N-)A-S-H gel) of S30 and S50 AASF paste are shown in Fig. 8(a) and (b). With the same M_s, S50 mixtures always have higher Ca/Si ratios than S30 ones due to a higher amount of Ca induced by increasing slag content. Additionally, the average Ca/Si ratio in sodium silicate-activated systems decline in both S30 and S50 mixtures with increasing activator M_s (0.5–1.5). Using sodium silicate-based activator introduces abundant Si species for further polymerization process, which could effectively reduce the Ca/Si ratio of the final reaction products [53]. Also, it is noteworthy that the mean Ca/Si ratio (in a range of 0.44–0.83) is consistent with previous studies of AASF [4,5,54], although they are considerably lower when compared with that in sodium-silicate activated slag [47,55], which is due to the fly ash incorporation.

In the sodium hydroxide-activated system, however, the mixture of S30M0 and S50M0 shows relatively lower Ca/Si when compared with S30M0.5 and S50M0.5 mixtures, respectively. Here, it is believed that the very early age reaction plays a crucial role in determining the Ca/Si
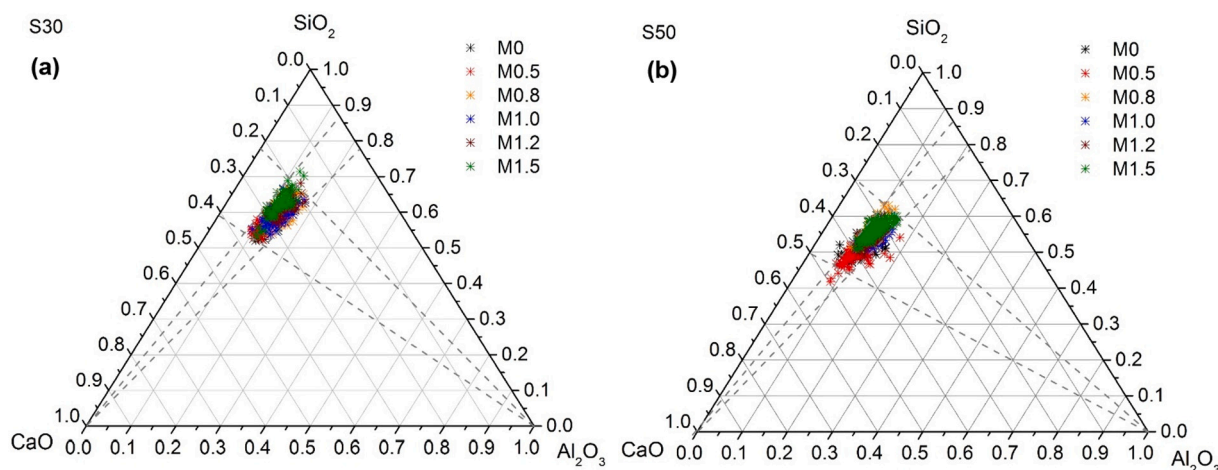

Fig. 6. Ternary diagram of CaO-SiO$_2$-Al$_2$O$_3$ of EDX spot analysis for the reaction products in (a) S30 and (b) S50 AASF pastes.
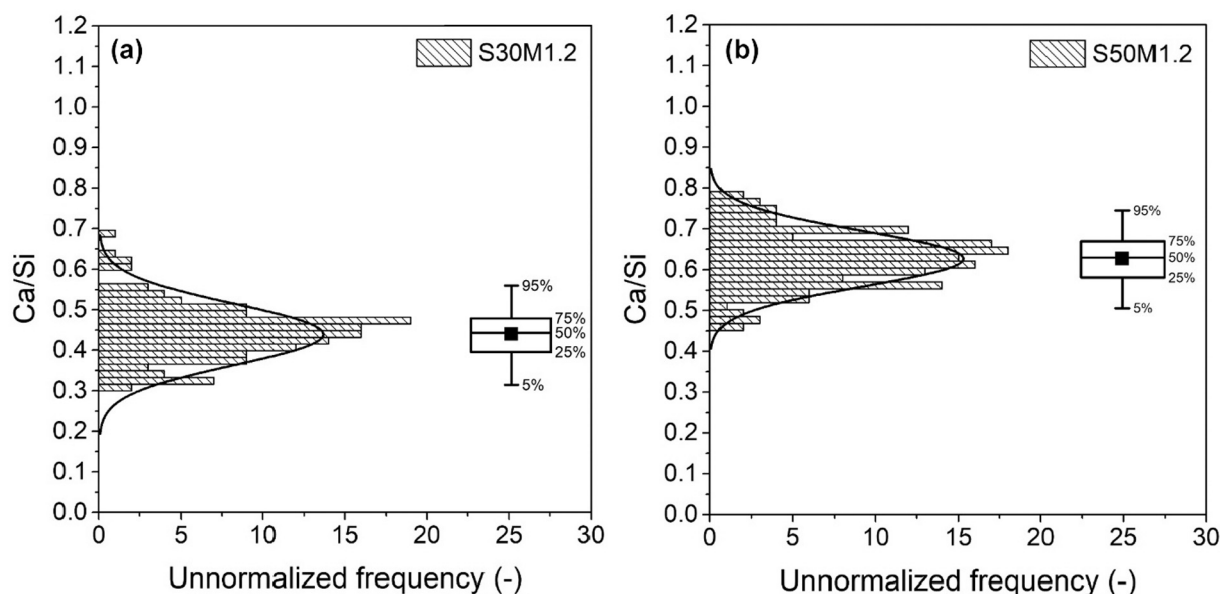
Fig. 7. Histogram and box plot of EDX data points (Ca/Si ratio) of the reaction products in (a) S30 and (b) S50 paste. In the box plot, the median value (–), the mean (■), the values at 25% and 75% (box edges), and the values at 5% and 95% level (whiskers) are illustrated.
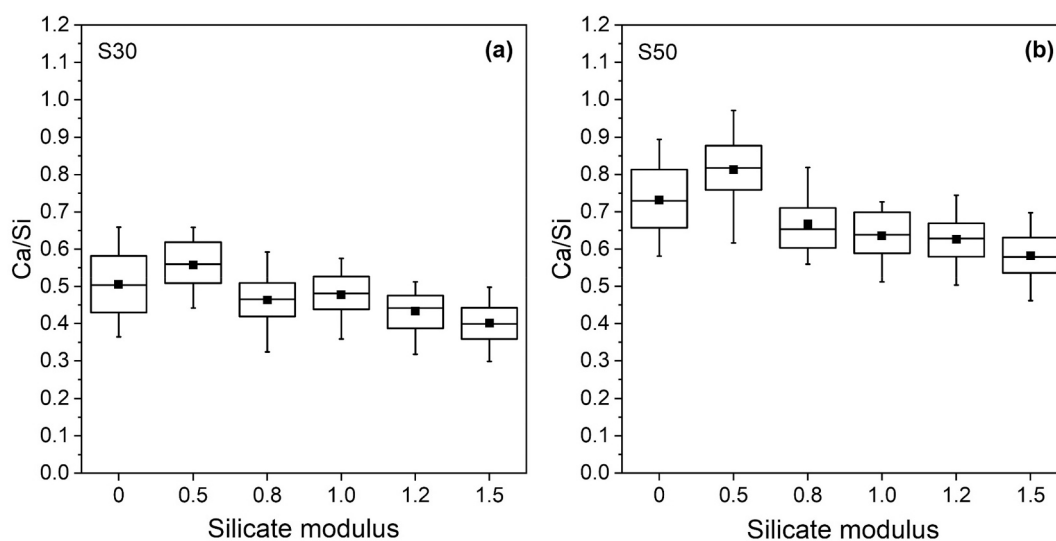

Fig. 8. Box plot of Ca/Si ratio of main reaction products in (a) S30 and (b) S50 AASF pastes. In the box plot, the median value (–), the mean (■), the values at 25% and 75% (box edges), and the values at 5% and 95% level (whiskers) are illustrated.

of the C-(N-)A-S-H gel. In comparison to sodium silicate-based activator with the same Na_2O content, the sodium hydroxide-based activator has evident higher alkalinity, which could inhibit the dissolution of Ca [56,57] while at the same time facilitate the dissolution of Si species from solid precursors, especially fly ash [53,57]. These effects consequently lead to a higher polymerization degree of the reaction products in S30M0 and S50M0 and an increase of crystallinity of C-(N-)A-S-H gel [48], which are the main reasons for the lower Ca/Si of the reaction product in S30M0 and S50M0. In fact, the increased polymerization degree has also been identified by FTIR analysis in this study (Section 3.3.2). Additionally, it is worth noting that a remark decrease of the Ca/Si ratio was previously detected from the slag particle to the reaction products within the AAS system [53]. Since the EDX point analyses were conducted on the "cloud edge" of the reaction products away from the slag particles, the Ca/Si ratio in the bulk region, therefore, could be relatively lower than the average gel composition. This effect tends to be more evident in sodium hydroxide-activated systems due to the

inhomogeneous distribution of the reaction products in comparison to sodium silicate-activated systems.

Finally, with increasing M_s, a similar trend of Ca/Si ratio of reaction products in both S30 and S50 was identified when compared to that of K_{Ic} (J_{tip}) in Fig. 4. Thus, it is believed that the fracture properties of AASF are strongly related to its reaction product chemistry reflected by the Ca/Si ratio as an indicator. Such a hypothesis is further discussed in Section 3.4.3.

3.3.2. FTIR analysis

The FTIR spectra of S30 and S50 AASF paste mixture at 28 days within the wavenumber range of 600 to 2000 cm^{-1} are shown in Fig. 9 (a) and (b), respectively. Both series of spectra indicate traces of quartz at 777 cm^{-1} and 796 cm^{-1} [58], which are identified as the remnant crystalline phases from incompletely reacted fly ash particles. The bands located near 660 cm^{-1} can be assigned to the deformational vibrations of Si—O—Si bonds with less crosslinking or stretching vibrations of
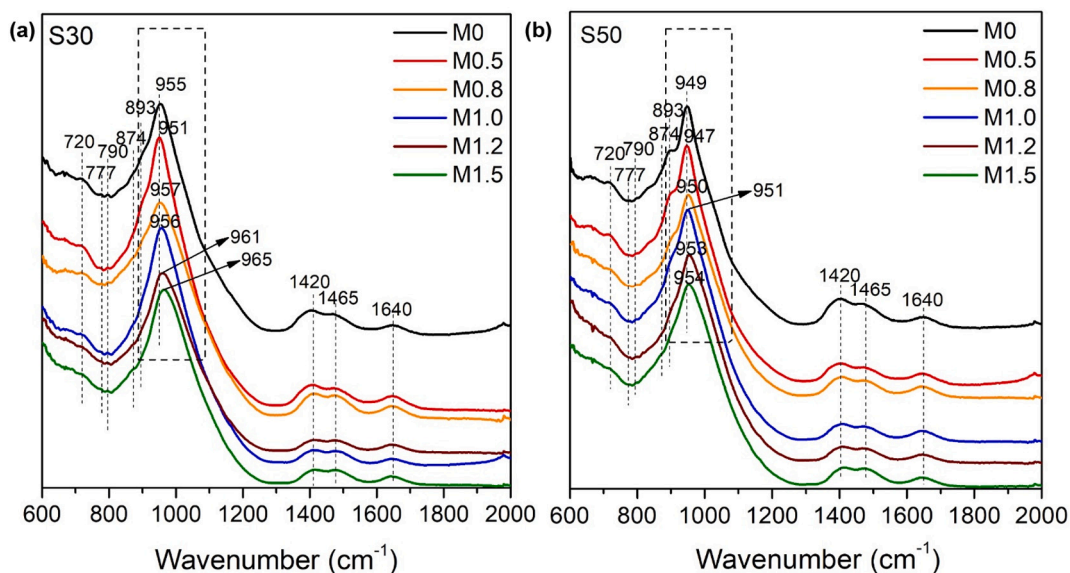
Fig. 9. FTIR spectra of (a) S30 and (b) S50 AASF pastes at 28 days.

Si—O—Al bonds [59,60]. The peak shoulder at 893 cm^{-1} is believed to be associated with stretching of Si—O with one non-bridging oxygen (NBO) per SiO_4 tetrahedral, which has been found in both unreacted slag and fly ash [61]. In addition, the peaks at 720 cm^{-1}, 874 cm^{-1} and the relative broad humps at 1420 cm^{-1} and 1465 cm^{-1} are associated with the presence of carbonate (CO_3^{2-}) with different vibration modes, which includes $\nu_4[CO_3]^{2-}$ for 720 cm^{-1}, $\nu_2[CO_3]^{2-}$ for 874 cm^{-1}, and $\nu_3[CO_3]^{2-}$ for 1420 cm^{-1} and 1465 cm^{-1} [62]. Additionally, the vibration bands detected near 3400 cm^{-1} and 1650 cm^{-1} are related to the bending vibrations of molecular water and a-/symmetric stretching of O—H bonds, respectively. Although the ones near 3400 cm^{-1} are not shown in Fig. 9.

More importantly, the overall broad band of interest is located between 800 and 1200 cm^{-1} as a result of phase overlapping from both precursors and reaction products. This band is widely accepted in the literature as the main T—O asymmetric stretching band and is used to study the changes of the amorphous gel structure (Ca/Si or Al/Si ratio) in AAMs [18,63–65]. Despite the influence of slag content, the main band of all spectra is centered at approximately 950 cm^{-1}, which is assigned to Si—O and/or Si—O—M bonds (M being alkali metal or alkali earth metal) [66]. More specifically, it could be associated with the Si—O—Si bonds of SiO_n units (n = 2) [67], which is the representative structure of (alumino)silicate chains-containing C-A-S-H type gel. This notably is in line with the EDX analysis, which confirms the formation of C-(N-)A-S-H gel as the main reaction product in all investigated AASF systems [4–6,21]. Additionally, the FTIR analysis detects no evident signal of Si-O-T (T being Si or Al) stretching with wavenumber higher than 1000 cm^{-1}, which are normally attributed to the three-dimensionally structured N-A-S-H type gels within fly ash and metakaolin-based geopolymers [68,69]. Considering the high amount of Ca^{2+} introduced by slag, the formation of N-A-S-H type gel in AASF system is not favored in comparison to C-A-S-H type gels [65]. Compatibility study of two types of gels also indicates the transformation of N-A-S-H to C-A-S-H under the environment of high pH when a considerable amount of Ca is present [65].

From the analysis of the main T—O band positions near 950 cm^{-1} in both S30 and S50 series, the shifts of the main T-O band are detected, which are depicted in Fig. 10. On one hand, higher slag content in AASF results in the T-O band with a lower wavenumber. On the other hand, the activator M_s also have a substantial influence on the position of the main T-O band of AASF paste. The wavenumber of the main T-O band increases with lower slag content but does not monotonically increase
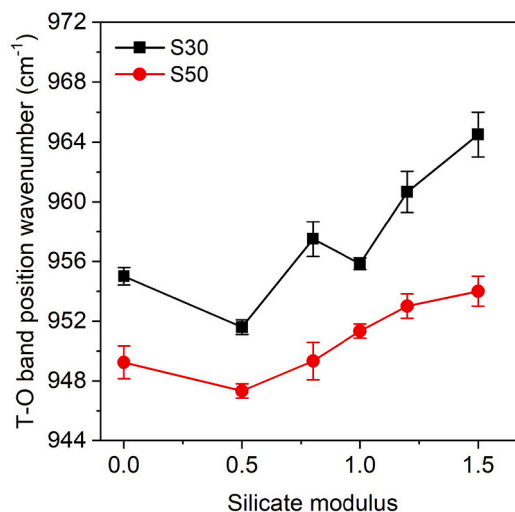

Fig. 10. Changes in wavenumber of the main T-O band for S30 and S50 pastes as a function of activator silicate modulus.

with increasing M_s. It first decreases from M_s 0 to 0.5 before the gradual increase. These position changes could be related to (i) the different levels of Al incorporation into the reaction product; and/or (ii) the different Ca/Si in the C-(N-)A-S-H gel as the main reaction product [18]. Indeed, the substitution of Si by Al in the Si-O-Si bonds in the reaction product results in the main T-O band shifting to lower numbers [18,69,70]. However, the first assumption is highly improbable since by increasing slag content, i.e. decreasing the fly ash content, the reactive alumina content within the binder does not change significantly. More significant variations are the available Ca^{2+} by changing the slag content and the available silica by changing the activator M_s. In particular, the amount of available silica (monomer in particular) and the pH of the activator change remarkably with different M_s [71,72]. These changes thereby have a major influence on the early age dissolution of solid precursors and effectively alter the apparent activation energy of AASF as well as the polymerization process of the C-(N-)A-S-H gel as the main reaction product [48]. Consequently, different final structures of C-(N-)A-S-H gel are anticipated. In fact, such main band shifting is also reported in cementitious systems as hydration proceeds and indicates a

higher polymerization degree and/or higher cross-linking of silica network in C-S-H gel and C-A-S-H gel [18,73]. Thus, it is believed the changes in wavenumber of the main band here are mainly determined by the polymerization/cross-linking of the silica-rich network in C-(N-)A-S-H gel. Interestingly, the trend of the main T-O band position with increasing M_s seems to share exactly the opposite trend with K_{Ic} (J_{tip}) (Fig. 4) as well as Ca/Si ratio (Fig. 8). Notably, the M0.5 mixtures with the lowest T-O band wavenumber, i.e. lowest polymerization degree, actually have the highest Ca/Si ratio as well as the highest K_{Ic} (J_{tip}). These correlations are considered uncoincidental and are discussed further in Sections 3.4.1 and 3.4.3.

3.3.3. Pore structure analysis

From the preliminary study using mercury intrusion porosimetry (MIP) and other research techniques [50], AASF paste has a very fine pore structure. The capillary pores larger than 0.1 μm are hardly observed particularly in silicate-activated systems. It thereby matches well with the pore structure range assessed with the nitrogen adsorption method, which covers the pore size from 0.002 to 0.1 μm.

The pore volume and pore size distribution of AASF paste derived from nitrogen adsorption are shown in Fig. 11(a) and (b), respectively. On one hand, AASF paste with higher slag content shows lower cumulative pore volume, i.e. porosity within the pore range from 0.002 to 0.1 μm, indicating the formation of a denser structure. On the other hand, in both S30 and S50 series, the cumulative pore volume first increases, peaks at M_s 1.0, and then decreases, which is consistent with the compressive strength development. Furthermore, the refinement of the pore structure with increasing M_s from 0 to 1.5 and increasing slag content could be clearly observed in Fig. 11(b), which is reflected by shifts of the critical pore size to smaller values in the pore size distribution curves. Notably, the pore structure of M0 and M0.5 mixtures is dominated by capillary pores larger than 0.01 μm. In contrast, the majority of pores in M1.0 and M1.5 mixtures belong to gel pores smaller than 0.01 μm.

Since the capillary pores defined as pores with size above 0.01 μm have a major impact on strength [74], the capillary porosity (>0.01 μm) is selected as an indicator to study the compressive strength of the AASF paste and the results are illustrated in Fig. 12. When compared with Fig. 2(a), it is clear that the trend of capillary porosity (>0.01 μm) coincides well with the compressive strength of AASF paste. This strong correlation between the compressive strength development and the capillary porosity is discussed in detail in Section 3.4.2.

3.3.4. Thermogravimetric analysis

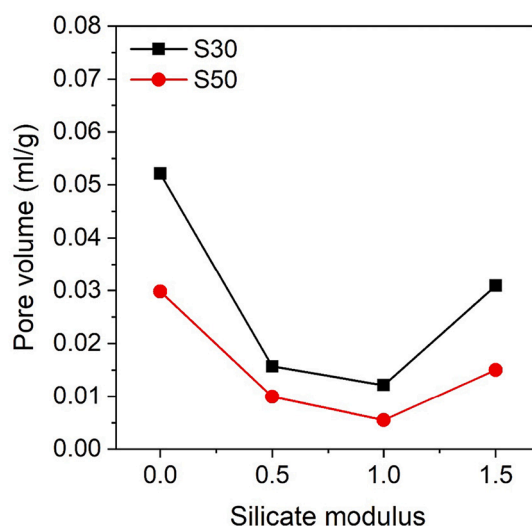The mass loss determined using thermogravimetry (TG) and the

Fig. 12. Capillary porosity (>0.01 μm) of AASF pastes at 28 days as a function of activator silicate modulus 0, 0.5, 1.0, and 1.5.

corresponding differential thermogravimetry (DTG) results are illustrated in Fig. 13 for AASF paste at 28 days. The mass loss within the range of 40 °C to 105 °C associated with the physically-bounded water is negligible due to the prior isopropanol solvent exchange. Major DTG peaks associated with decomposition of the main reaction product for all samples are found between 105 and 300 °C. Following the EDX analysis in Section 3.3.1, the mass loss within this range in all investigated mixtures is associated with C-(N-)A-S-H gel as the main reaction product. Furthermore, this range agrees well with the C-S-H gel in cementitious systems [75,76] or the C-A-S-H type gel [65,77], as well as the C-(N-)A-S-H gel in AAS [48,78] and AASF system [4,18,21]. Additionally, the minor DTG peaks present at 300 to 400 °C in Fig. 13 are attributed to the dehydration process of the hydrotalcite phase [4,79,80], which includes interlayer water loss up to 270 °C and dehydration of the main layer at approximately 400 °C. The presence of the hydrotalcite phase is also in line with many previous experimental and thermodynamics modeling studies of alkali-activated binders with slag as the major solid precursor [4,18,48,49]. Finally, very weak peaks observed between 500 and 800 °C are mainly due to the carbonated phases. Above 800 °C, new phases start to crystallize under high temperature and the process could be dominated by the formation of akermanite as reported by other researchers [81].
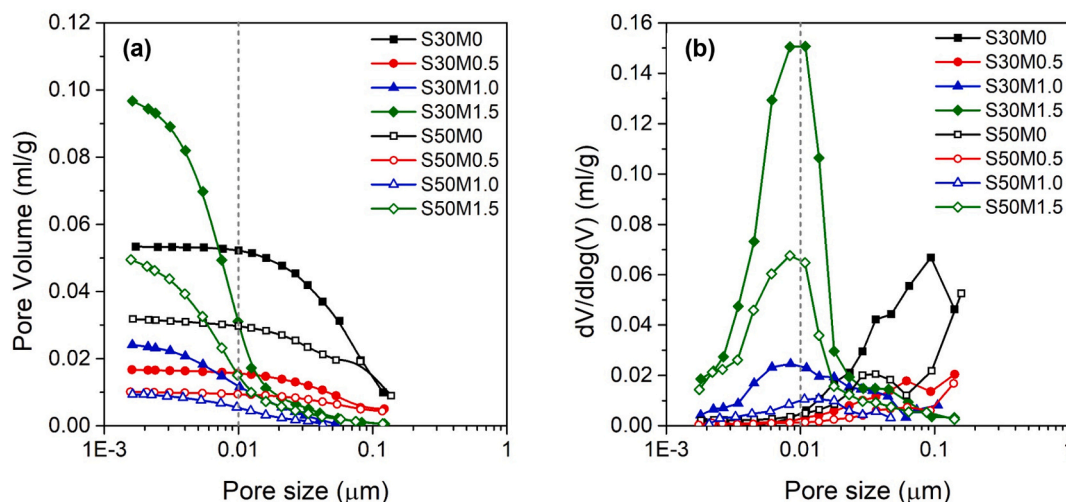
Fig. 11. (a) Cumulative pore volume and (b) pore size distribution of AASF pastes at 28 days derived from nitrogen adsorption tests.
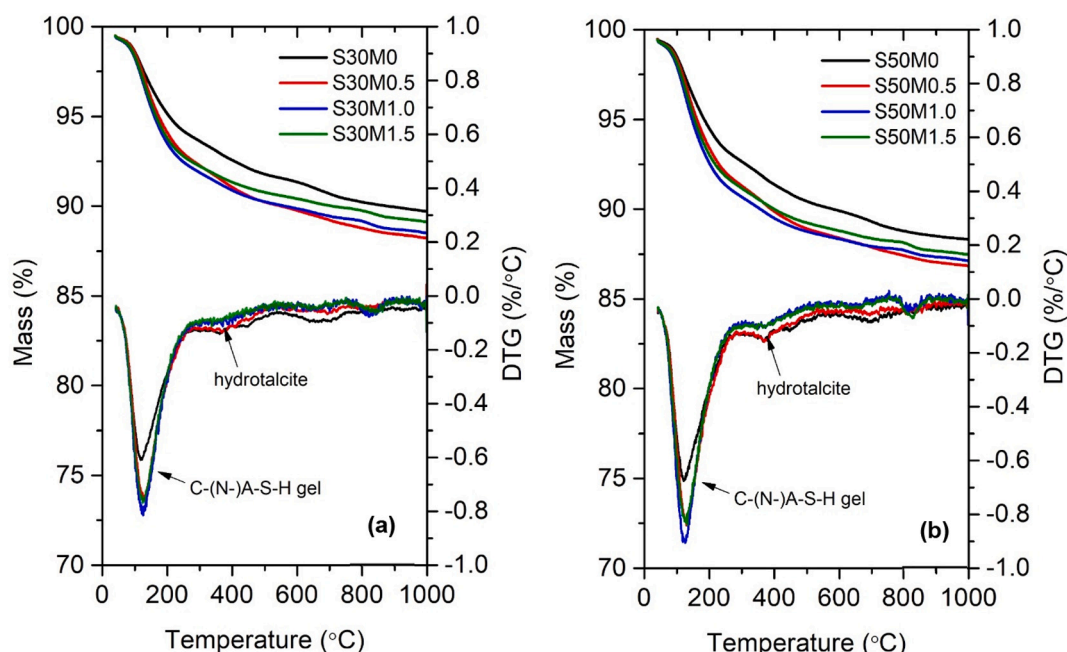
Fig. 13. Thermogravimetric (TG) and differential thermogravimetric (DTG) curves of (a) S30 and (b) S50 pastes at 28 days.
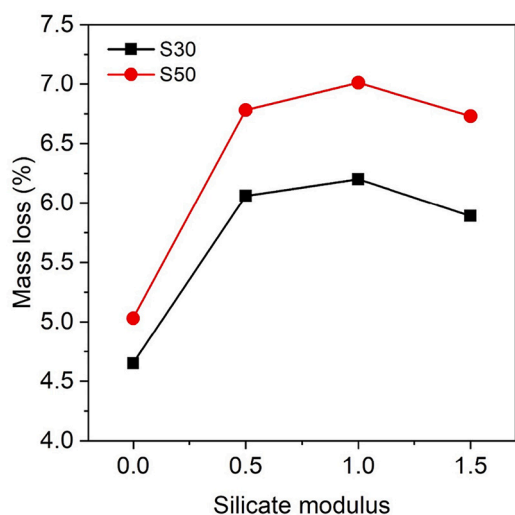

Fig. 14. Mass loss of the main reaction product within temperature range 105 to 300 °C in AASF pastes at 28 days.

Fig. 15. Correlations of Ca/Si ratio of C-(N-)A-S-H gel as main reaction product and the position of main T-O vibration band in FTIR.

Assuming that C-(N-)A-S-H gel is the dominant binding phase in AASF, its amount could be inferred from the percentage of mass loss from 105 to 300 °C on the thermogravimetric (TG) curves in Fig. 13. Accordingly, the mass loss in the range of 105–300 °C of all investigated mixtures at 28 days is plotted in Fig. 14. It is clear that the slag content has a significant impact on the formation of reaction products, mixtures with higher slag content have evident higher mass loss at the same M_s. Furthermore, M_s also plays a major role in determining the amount of reaction product formation. It is observed here that the trend of reaction product mass loss coincides well with the compressive strength of AASF paste, which is also exactly the opposite of the porosity results given in Fig. 12. This evidence suggests that the different amount of reaction product formation leads to changes in the porosity of AASF pastes, which consequently determines the mixture compressive strength. Such correlations are further discussed in Section 3.4.2.
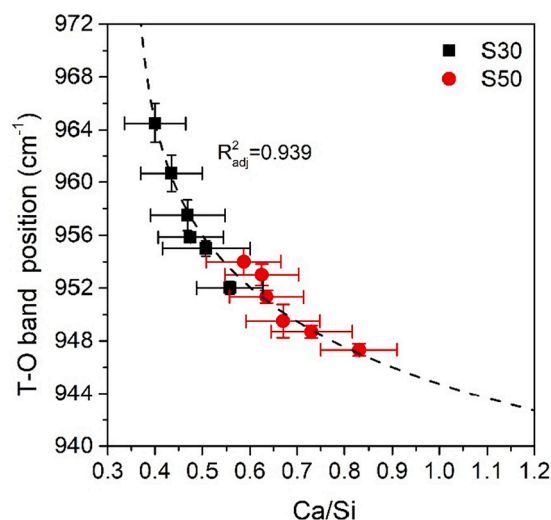
3.4. General discussions

3.4.1. Polymerization degree of C-(N-)A-S-H gel in AASF

As previously mentioned in Section 3.3.2, evident correlations were observed between the Ca/Si ratio of the reaction product and corresponding polymerization degree as reflected by the position of the main T-O band, which is shown in Fig. 15. With increasing Ca/Si, the position of the main T-O band and the related polymerization degree of the C-(N-)A-S-H gel has a hyperbolic decrease. This trend is reasonable for C-S-H/C-A-S-H type gel because the higher Ca/Si, according to previous research, normally relates to less polymerized C-A-S-H structure, which is primarily associated with shorter mean chain length (MCL) of aluminosilicate chains (Q^2) as well as fewer crosslinking cites (Q^3) [82]. In fact, the relationship between the position of the main T-O band (as an indication of the polymerization degree) and Ca/Si shares an identical trend with MCL vs Ca/Si in the previous experimental study of C-S-H

[83] and thermodynamics modeling C-(N-)A-S-H gel in AAS [84]. Additionally, the relationship between decreasing Ca/Si ratio and increased polymerization degree of C-(N-)A-S-H were also identified during the carbonation process of AAS and AASF paste due to the decalcification [54]. The correlation depicted in Fig. 15 thus strongly indicates that the polymerization degree of C-(N-)A-S-H gel formed in AASF paste, similar to that of C-S-H/C-A-S-H gel, is also substantially governed by its Ca/Si ratio. It should also be noted here that this correlation between polymerization degree and Ca/Si ratio reflects what is believed to be the intrinsic property of the C-(N-)A-S-H gel, which is independent from the mixture preparation route including slag content as well as activator M_s.

3.4.2. Compressive strength of AASF paste and the pore structure

Following results from the pore structure, the correlation identified between compressive strength and corresponding capillary porosity (>0.01 μm) is plotted in Fig. 16(a). A Ryshkevitch exponential model [85] was applied considering porosity as the single parameter, which fits the relationship of the compressive strength of AASF paste and its capillary porosity (>0.01 μm). A correlation coefficient R_{adj}^2 is determined to be 0.825 as shown in Fig. 16(a), indicating the compressive strength is strongly dependent on the capillary porosity (>0.01 μm) of AASF paste.

Furthermore, this study also identified the strong linear correlation between the mass loss of C-(N-)A-S-H gel and the corresponding compressive strength of AASF paste, which indicates a positive correlation between the amount of gel phases formation and the compressive strength of AASF paste. This relationship between compressive strength and corresponding mass loss of the reaction product is illustrated in Fig. 16(b). Considering the same solid precursor combination and w/b ratio used for mixture preparation, the mixtures in S30 and S50 series accordingly should have similar initial particle packing. Under such circumstances, a higher amount of C-(N-)A-S-H gel formation could lead to lower porosity and higher gel/space ratio, which thereby result in a higher compressive strength [86,87]. Consensually, the porosity-based theory treating pores within materials as weakest links still proves valid to explain the compressive strength development of AASF paste, which agrees with previous studies [88,89].

3.4.3. Fracture properties of AASF paste and the Ca/Si ratio of the reaction product

Several hypotheses have been developed by previous studies to explain the factors determining the mechanical properties of

cementitious materials, which include (I) the porosity, (II) the phase assemblage, and (III) the cohesion/adhesion-based theory [90]. Fracture properties of AASF, as one of the mechanical properties, should fall into one or more of these three categories. As discussed earlier, although the porosity-based theory is quite compatible to explain the compressive strength development, it seems invalid for K_{Ic} (J_{tip}). In fact, no evident correlations between the capillary porosity (>0.01 μm) and K_{Ic} (J_{tip}) were identified in this study.

The influence of phase assemblage, on the other hand, could be prominently reflected by the intrinsic mechanical properties of principal phases (including elastic modulus, tensile strength, etc.) in one system. In AASF, the main binding phase is the C-(N-)A-S-H gel with variable chemical composition and atomic structure, which could be indicated by its average Ca/Si ratio. Compared to the average Ca/(Si+Al) or Al/Si ratio, the average Ca/Si ratio is used here to ensure the minimization of the influence by unreacted precursor particles as well as hydrotalcite formed as the secondary reaction product. Therefore, the K_{Ic} and J_{tip} as the fracture properties were plot against the corresponding Ca/Si ratio of the reaction product in Fig. 17(a). A strong linear relationship was discovered between K_{Ic} as a function of corresponding Ca/Si in AASF paste. Besides, a good hyperbolic relationship between J_{tip} and corresponding Ca/Si could be also observed in Fig. 17(b). Both these two relationships suggest the fracture properties K_{Ic} (J_{tip}) of AASF pastes are dominated by and positively related to the Ca/Si ratio of C-(N-)A-S-H gel as the main reaction product. As shown in FTIR Fig. 15, a higher polymerization/crosslinking degree, i.e. a longer mean chain length (MCL), is well correlated with a lower Ca/Si ratio of C-(N-)A-S-H gel [91]. Furthermore, it has been intensively reported that the decline of the Ca/Si ratio enhances the nanoscale intrinsic mechanical properties of C-S-H/C-A-S-H type gel, which includes its tensile strength and elastic modulus as suggested by [92–94]. This trend, however, is exactly the opposite when compared with K_{Ic} (J_{tip}) as a function of Ca/Si. Such proof by contradiction thereby indicates that instead of the phase assemblage (the intrinsic mechanical properties of C-(N-)A-S-H gel) that governs the K_{Ic} (J_{tip}) of AASF, the dominant factors lie outside the nanoscale structure of the C-(N-)A-S-H phase.

Consequently, it seems only reasonable to hypothesize that both K_{Ic} and J_{tip} are determined by a cohesion/adhesion-based mechanism, which includes either the cohesion between the C-(N-)A-S-H gel particles (globules), and/or partially by the adhesion properties between the C-(N-)A-S-H gel particles (globules) and the remnant slag and fly ash particles [95]. This hypothesis is considered not based on simple speculation, but rather by substantiated indirect experimental evidence as
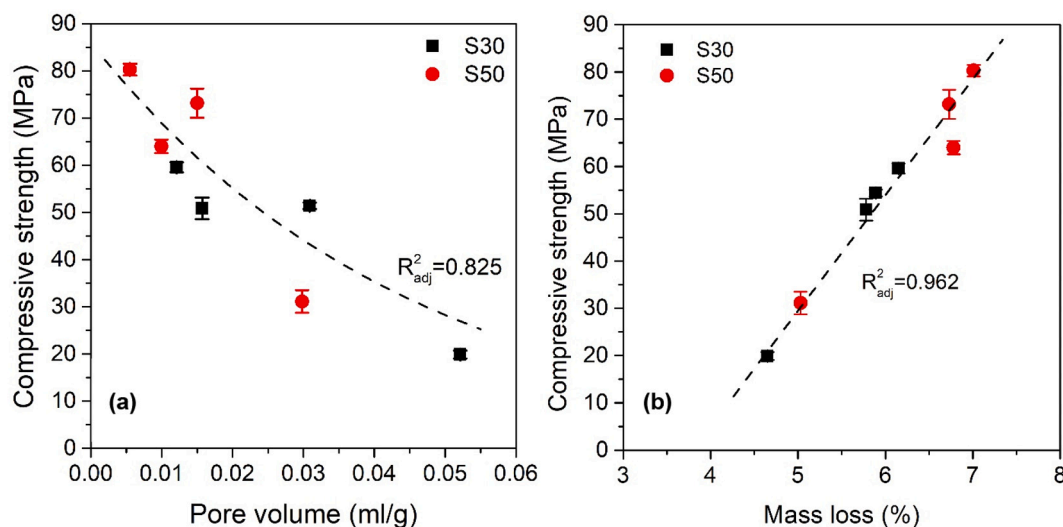

Fig. 16. (a) Correlation between compressive strength and capillary porosity (>0.01 μm) and (b) between compressive strength and mass loss of main reaction product.
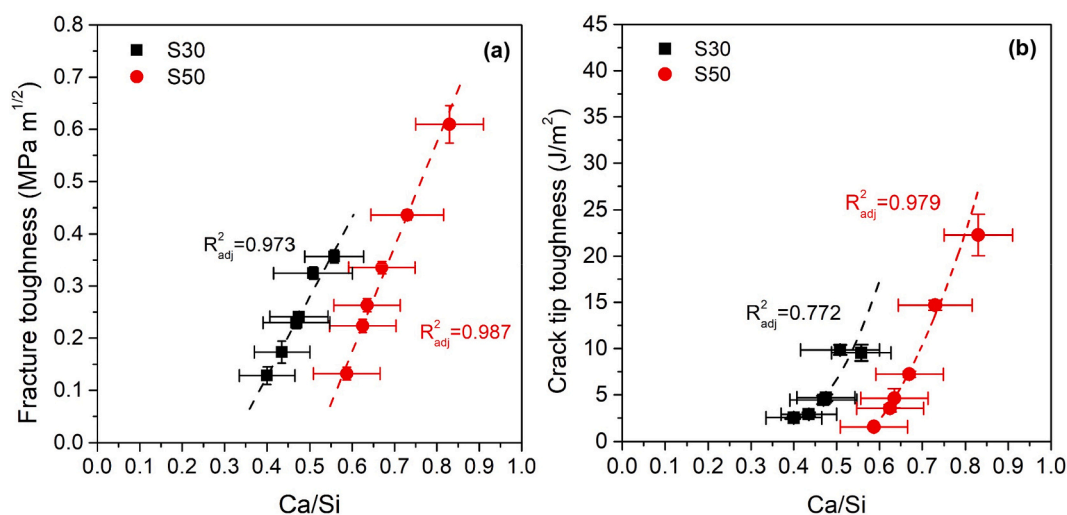
Fig. 17. Correlation of (a) fracture toughness K_{Ic} and (b) crack tip toughness J_{tip} as a function of the Ca/Si ratio of C-(N-)A-S-H gel as the main reaction product of AASF pastes.
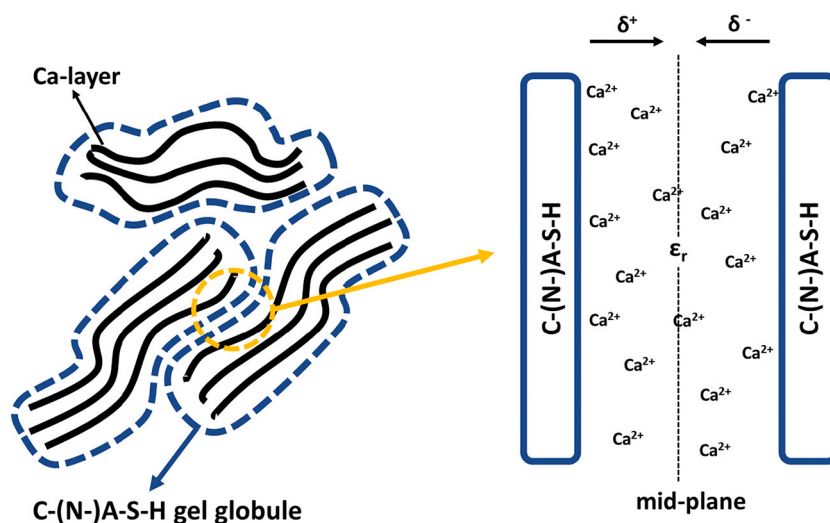

Fig. 18. Schematic representation of cohesion mechanism between C-(N-)A-S-H particles (globules), the atomic structure of which is ignored and represented by uniformly charge walls separated by a dielectric continuum in which Ca^{2+} ions are free to move (adopted from [102]).

well as verified theories by previous researchers. Both the cohesion between and/or the adhesion is considered an essential component of the mechanical properties of cementitious materials [95,96], which have been experimentally confirmed using atomic force microscopy [97] as well as zeta potential measurements [98]. In AASF, these strong interactions between two solid surfaces (treated as homogeneously charged walls) are believed to be similar to those between C-S-H particles in cement paste, which is a result of ion-ion correlation interactions caused by very high negatively charged C-(N-)A-S-H particles (globules) and the presence of Ca^{2+} as divalent counterions [95,97]. Based on this, a schematic representation of cohesion between C-(N-)A-S-H gel particles (globules) is illustrated in Fig. 18. C-(N-)A-S-H gel with a higher Ca/ Si ratio also has a higher negatively surface charge density [99], which effectively enhance the cohesion between the C-(N-)A-S-H particles (globules) under the presence of abundant Ca^{2+} ions which are free to move. These configurations under a higher Ca/Si ratio of C-(N-)A-S-H consequently provide higher resistance for crack initiation and propagation process, which is reflected by the higher K_{Ic} (J_{tip}) of corresponding mixtures. On the other hand, the unreacted precursor particles, mainly crystalline quartz and mullite phases in fly ash

particles, share similar surface charge properties with C-S-H [98,100]. Accordingly, the adhesion between C-(N-)A-S-H particles (globules) and unreacted precursor particles also have a similar mechanism as the cohesion in between C-(N-)A-S-H particles (globules), and the adhesion enhances with increasing Ca/Si as well, as supported by previous findings on adhesion mechanism between filler (quartz) and C-S-H [98]. Still, it is worth noting here the gel porosity (<0.01 μm) of C-(N-)A-S-H gel could affect the cohesion/adhesion considering the gel pores and the elementary C-(N-)A-S-H particle (globules) are at similar length scale [101]. However, the correlation between the K_{Ic} (J_{tip}) and the gel porosity (<0.01 μm) is much weaker compared to that between the K_{Ic} (J_{tip}) and the Ca/Si ratio. Consequently, although the general influence of gel porosity on the fracture properties cannot be excluded, the cohesion/adhesion is still considered as the dominating mechanism for fracture properties of AASF pastes.

This strong correlation between Ca/Si as an indicator of cohesion and adhesion and K_{Ic} (J_{tip}) gives promising guidance for fine-tuning the fracture properties by only minor modification of the mixture design. These modifications could involve the changing of activator M_s (Si) as well as the slag content (Ca). The findings in this study are particularly

valuable for the mixture design that requires accurate engineering of its fracture properties for satisfactory composite performance, such as strain hardening geopolymer/cementitious composite. Finally, it is crucial to note that the hypothesized cohesion/adhesion-based mechanism is supported by indirect evidence of reaction product chemistry found in this study. Molecular dynamics simulations and direct measurements of ion-ion correlation interactions between C-(N-)A-S-H particles (globules) as well as C-(N-)A-S-H particles (globules) and remnant precursor particles are recommended for future research.

4. Conclusions

This study presents a comprehensive experimental investigation on the fracture properties and microstructure formation of hardened AASF paste, which were prepared with various slag/fly ash mass ratios and silicate modulus (M_s) of alkaline activator. Strong correlations between reaction product chemical composition and fracture properties of AASF paste were identified. The following conclusions are drawn from the results of this study:

- An increase of slag content in AASF paste results in superior mechanical properties, including compressive strength, elastic modulus as well as fracture toughness K_{Ic}/crack tip toughness J_{tip}. In comparison to the sodium hydroxide-based activator, the sodium silicate-based activator effectively enhances the mechanical properties of AASF. However, increasing M_s of alkaline activator does not lead to a monotonic increase of mechanical properties and the optimal activation condition is achieved by using moderate M_s.
- The compressive strength of AASF paste is primarily determined by its capillary porosity ($>0.01\ \mu m$), which is compatible with the generally accepted porosity-based theory for conventional cementitious materials.
- The polymerization degree of C-(N-)A-S-H gel, indicated by the position of the main T-O band of AASF paste, is substantially governed by its Ca/Si ratio.
- Strong positive correlations are identified between the Ca/Si ratio of C-(N-)A-S-H gel and the fracture properties K_{Ic} (J_{tip}) of AASF pastes.
- Despite the influence of the gel porosity ($<0.01\ \mu m$), disagreements are found between the Ca/Si ratios and corresponding intrinsic mechanical properties of the C-(N-)A-S-H gel. This proof by contradiction indicates that the fracture properties K_{Ic} (J_{tip}) of AASF pastes could be dominated by a cohesion/adhesion-based mechanism.
- This study provides promising guidance for fine-tuning the fracture properties of AASF. Further, it also contributes to the tailoring strategies for high-performance composite, for instance, SHGC, through proper mixture design.

CRediT authorship contribution statement

Shizhe Zhang: Conceptualization, Methodology, Investigation, Formal analysis, Writing - Original Draft, Writing - Review & Editing Zhenming Li: Investigation, Writing - Review & Editing Bahman Ghiassi: Methodology, Writing - Review & Editing Suhong Yin: Writing - Review & Editing, Funding acquisition Guang Ye: Supervision, Writing - Review & Editing, Project administration, Funding acquisition.

Declaration of competing interest

The authors declare that there is no conflict of interest.

Acknowledgements

References

[1] C. Shi, D. Roy, P. Krivenko, Alkali-activated Cements and Concretes, CRC press, 2006.

[2] G. Habert, C. Ouellet-Plamondon, Recent update on the environmental impact of geopolymers, in: RILEM Technical Letters vol. 1, 2016, pp. 17–23.

[3] P. Duxson, J.L. Provis, G.C. Lukey, J.S. Van Deventer, The role of inorganic polymer technology in the development of 'green concrete', Cem. Concr. Res. 37 (2007) 1590–1597.

[4] I. Ismail, S.A. Bernal, J.L. Provis, R. San Nicolas, S. Hamdan, J.S. van Deventer, Modification of phase evolution in alkali-activated blast furnace slag by the incorporation of fly ash, Cem. Concr. Compos. 45 (2014) 125–135.

[5] F. Puertas, A. Fernández-Jiménez, Mineralogical and microstructural characterisation of alkali-activated fly ash/slag pastes, Cem. Concr. Compos. 25 (2003) 287–292.

[6] N.K. Lee, H.K. Lee, Reactivity and reaction products of alkali-activated, fly ash/slag paste, Constr. Build. Mater. 81 (2015) 303–312.

[7] S. Puligilla, P. Mondal, Role of slag in microstructural development and hardening of fly ash-slag geopolymer, Cem. Concr. Res. 43 (2013) 70–80.

[8] K.L. Scrivener, V.M. John, E.M. Gartner, Eco-efficient cements: potential economically viable solutions for a low-CO₂ cement-based materials industry, Cem. Concr. Res. 114 (2018) 2–26.

[9] P. Nath, P.K. Sarker, Fracture properties of GGBFS-blended fly ash geopolymer concrete cured in ambient temperature, Mater. Struct. 50 (2016) 32.

[10] Y. Ding, C.-J. Shi, N. Li, Fracture properties of slag/fly ash-based geopolymer concrete cured in ambient temperature, Constr. Build. Mater. 190 (2018) 787–795.

[11] Z. Pan, J.G. Sanjayan, B.V. Rangan, Fracture properties of geopolymer paste and concrete, Mag. Concr. Res. 63 (2011) 763–771.

[12] V.C. Li, H.-C. Wu, Conditions for pseudo strain-hardening in fiber reinforced brittle matrix composites, Appl. Mech. Rev. 45 (1992) 390–398.

[13] M. Ohno, V.C. Li, An integrated design method of Engineered Geopolymer Composite, Cem. Concr. Compos. 88 (2018) 73–85.

[14] S. Zhang, V.C. Li, G. Ye, Micromechanics-guided development of a slag/fly ash-based strain-hardening geopolymer composite, Cem. Concr. Compos. 109 (2020) 103510.

[15] B. Nematollahi, J. Sanjayan, F.U.A. Shaikh, Matrix design of strain hardening fiber reinforced engineered geopolymer composite, Compos. Part B 89 (2016) 253–265.

[16] M.E. Launey, R.O. Ritchie, On the fracture toughness of advanced materials, Adv. Mater. 21 (2009) 2103–2110.

[17] ASTM, C618, Standard Specification for Fly Ash and Raw or Calcined Natural Pozzolan for Use as a Mineral Admixture in Portland Cement Concrete, C618, 2003.

[18] S. Zhang, A. Keulen, K. Arbi, G. Ye, Waste glass as partial mineral precursor in alkali-activated slag/fly ash system, Cem. Concr. Res. 102 (2017) 29–40.

[19] Y. Zuo, M. Nedeljković, G. Ye, Pore solution composition of alkali-activated slag/fly ash pastes, Cem. Concr. Res. 115 (2019) 230–250.

[20] S. Zhang, M. Nedeljković, B. Ghiassi, G. Ye, A comparative study on deflection-hardening behavior of ductile alkali-activated composite, in: International Conference on Strain-hardening Cement-based Composites, Springer, 2017, pp. 123–130.

[21] X. Gao, Q.L. Yu, H.J.H. Brouwers, Reaction kinetics, gel character and strength of ambient temperature cured alkali activated slag–fly ash blends, Constr. Build. Mater. 80 (2015) 105–115.

[22] S.A. Bernal, J.L. Provis, V. Rose, R. Mejía de Gutierrez, Evolution of binder structure in sodium silicate-activated slag-metakaolin blends, Cem. Concr. Compos. 33 (2011) 46–54.

[23] D. Ravikumar, N. Neithalath, Effects of activator characteristics on the reaction product formation in slag binders activated using alkali silicate powder and NaOH, Cem. Concr. Compos. 34 (2012) 809–818.

[24] NEN, 196-1, Methods of Testing Cement–Part 1: Determination of Strength, European Committee for Standardization, 2005.

[25] ASTM, C 469 Standard Test Method for Static Modulus of Elasticity and Poisson's Ratio of Concrete in Compression, 2010.

[26] M. Irfan-ul-Hassan, B. Pichler, R. Reihsner, C. Hellmich, Elastic and creep properties of young cement paste, as determined from hourly repeated minute-long quasi-static tests, Cem. Concr. Res. 82 (2016) 36–49.

[27] TU1404, Cost Action: Towards the Next Generation of Standards for Service Life of Cement-based Materials and Structures, Main Phase of the Extended Round Robin Testing Programme Testing Protocols, 2016.

[28] Y. Zhu, S. Xu, Fracture properties of cement paste and mortar: an experimental investigation, in: Proceedings IA-FraMCoS-6, International Assoc. of Fracture Mech. for Concrete and Concrete Structures, Catania, Italy, 1–3, 2007, pp. 17–22.

[29] J. Standard, Method of Test for Fracture Energy of Concrete by Use of Notched Beam, JCI-S-001e2003, Japan Concrete Institute, 2003.

[30] J. Lee, M.M. Lopez, An experimental study on fracture energy of plain concrete, Int. J. Concr. Struct. Mater. 8 (2014) 129–139.

[31] F. Aslani, M. Bastami, Relationship between deflection and crack mouth opening displacement of self-compacting concrete beams with and without fibers, Mech. Adv. Mater. Struct. 22 (2015) 956–967.

[32] S. Zhao, W. Sun, D. Lange, Deflection–crack mouth opening displacement relationship for concrete beams with and without fibres, Mag. Concr. Res. 67 (2015) 532–540.

[33] G. Ye, Experimental Study and Numerical Simulation of the Development of the Microstructure and Permeability of Cementitious Materials, TU Delft, Delft University of Technology, 2003.

[34] X. Ouyang, Y. Ma, Z. Liu, J. Liang, G. Ye, Effect of the sodium silicate modulus and slag content on fresh and hardened properties of alkali-activated fly ash/slag, Minerals 10 (2020) 15.

[35] D. Ravikumar, N. Neithalath, Reaction kinetics in sodium silicate powder and liquid activated slag binders evaluated using isothermal calorimetry, Thermochim. Acta 546 (2012) 32–43.

[36] K. Kendall, A. Howard, J.D. Birchall, The relation between porosity, microstructure and strength, and the approach to advanced cement-based materials, Philos. Trans. R. Soc. Lond. A Math. Phys. Sci. 310 (1983) 139–153.

[37] R.A. Helmuth, D.H. Turk, Elastic Moduli of Hardened Portland Cement and Tricalcium Silicate Pastes: Effect of Porosity, 1966.

[38] B. Hillemeier, H.K. Hilsdorf, Fracture mechanics studies on concrete compounds, Cem. Concr. Res. 7 (1977) 523–535.

[39] T. Nishikawa, M. Takatsu, M. Daimon, Fracture behavior of hardened cement paste incorporating mineral additions, Cem. Concr. Res. 25 (1995) 1218–1224.

[40] D.A. Lange, H.M. Jennings, S.P. Shah, Relationship between fracture surface roughness and fracture behavior of cement paste and mortar, J. Am. Ceram. Soc. 76 (1993) 589–597.

[41] T. Ficker, D. Martišek, H.M. Jennings, Roughness of fracture surfaces and compressive strength of hydrated cement pastes, Cem. Concr. Res. 40 (2010) 947–955.

[42] K. Scrivener, R. Snellings, B. Lothenbach, A Practical Guide to Microstructural Analysis of Cementitious Materials, CRC Press, 2018.

[43] S.-D. Wang, K.L. Scrivener, Hydration products of alkali activated slag cement, Cem. Concr. Res. 25 (1995) 561–571.

[44] I. Richardson, A. Brough, G. Groves, C. Dobson, The characterization of hardened alkali-activated blast-furnace slag pastes and the nature of the calcium silicate hydrate (CSH) phase, Cem. Concr. Res. 24 (1994) 813–829.

[45] F. Puertas, S. Martínez-Ramírez, S. Alonso, T. Vazquez, Alkali-activated fly ash/slag cements: strength behaviour and hydration products, Cem. Concr. Res. 30 (2000) (1625-1632).

[46] E. Deir, B.S. Gebregziabiher, S. Peethamparan, Influence of starting material on the early age hydration kinetics, microstructure and composition of binding gel in alkali activated binder systems, Cem. Concr. Compos. 48 (2014) 108–117.

[47] F. Puertas, M. Palacios, H. Manzano, J.S. Dolado, A. Rico, J. Rodríguez, A model for the C-A-S-H gel formed in alkali-activated slag cements, J. Eur. Ceram. Soc. 31 (2011) 2043–2056.

[48] Y. Zuo, M. Nedeljković, G. Ye, Coupled thermodynamic modelling and experimental study of sodium hydroxide activated slag, Constr. Build. Mater. 188 (2018) 262–279.

[49] J.E. Oh, P.J.M. Monteiro, S.S. Jun, S. Choi, S.M. Clark, The evolution of strength and crystalline phases for alkali-activated ground blast furnace slag and fly ash-based geopolymers, Cem. Concr. Res. 40 (2010) 189–196.

[50] M. Nedeljković, B. Šavija, Y. Zuo, M. Luković, G. Ye, Effect of natural carbonation on the pore structure and elastic modulus of the alkali-activated fly ash and slag pastes, Constr. Build. Mater. 161 (2018) 687–704.

[51] J. Rossen, K. Scrivener, Optimization of SEM-EDS to determine the C–A–S–H composition in matured cement paste samples, Mater. Charact. 123 (2017) 294–306.

[52] K. Kjellsen, A. Monsøy, K. Isachsen, R. Detwiler, Preparation of flat-polished specimens for SEM-backscattered electron imaging and X-ray microanalysis—importance of epoxy impregnation, Cem. Concr. Res. 33 (2003) 611–616.

[53] H. Ye, A. Radlińska, Fly ash-slag interaction during alkaline activation: influence of activators on phase assemblage and microstructure formation, Constr. Build. Mater. 122 (2016) 594–606.

[54] M. Nedeljković, Carbonation Mechanism of Alkali-activated Fly Ash and Slag Materials: In View of Long-term Performance Predictions, Delft University of Technology, 2019.

[55] A.R. Brough, A. Atkinson, Sodium silicate-based, alkali-activated slag mortars: part I. Strength, hydration and microstructure, Cem. Concr. Res. 32 (2002) 865–879.

[56] S. Song, H.M. Jennings, Pore solution chemistry of alkali-activated ground granulated blast-furnace slag, Cem. Concr. Res. 29 (1999) 159–170.

[57] Y. Zuo, Experimental Study and Numerical Simulation of the Reaction Process and Microstructure Formation of Alkali-activated Materials, Delft University of Technology, 2019.

[58] D.P. Tuchman, Research toward Direct Analysis of Quartz Dust on Filters Using FTIR Spectroscopy, US Department of the Interior, Bureau of Mines, 1992.

[59] Z. Zhang, H. Wang, J.L. Provis, Quantitative study of the reactivity of fly ash in geopolymerization by FTIR, J. Sustain. Cem. Based Mater. 1 (2012) 154–166.

[60] I. García Lodeiro, D.E. Macphee, A. Palomo, A. Fernández-Jiménez, Effect of alkalis on fresh C–S–H gels. FTIR analysis, Cem. Concr. Res. 39 (2009) 147–153.

[61] S. Zhang, Waste Glass as Partial Binder Precursor and Fine Aggregate Replacement in Alkali Activated Slag/Fly Ash System, 2015.

[62] F.B. Reig, J.G. Adelantado, M.M. Moreno, FTIR quantitative analysis of calcium carbonate (calcite) and silica (quartz) mixtures using the constant ratio method. Application to geological samples, Talanta 58 (2002) 811–821.

[63] M. Criado, A. Fernández-Jiménez, A. Palomo, Alkali activation of fly ash: effect of SiO_2/Na_2O ratio: part I: FTIR study, Microporous Mesoporous Mater. 106 (2007) 180–191.

[64] I. García-Lodeiro, A. Fernández-Jiménez, M.T. Blanco, A. Palomo, FTIR study of the sol–gel synthesis of cementitious gels: C–S–H and N–A–S–H, J. Sol-Gel Sci. Technol. 45 (2008) 63–72.

[65] I. Garcia-Lodeiro, A. Palomo, A. Fernández-Jiménez, D.E. Macphee, Compatibility studies between N-A-S-H and C-A-S-H gels. Study in the ternary diagram Na2O–CaO–Al2O3–SiO2–H2O, Cem. Concr. Res. 41 (2011) 923–931.

[66] W. Lee, J. Van Deventer, Use of infrared spectroscopy to study geopolymerization of heterogeneous amorphous aluminosilicates, Langmuir 19 (2003) 8726–8734.

[67] N. Clayden, S. Esposito, A. Aronne, P. Pernice, Solid state 27 Al NMR and FTIR study of lanthanum aluminosilicate glasses, J. Non-Cryst. Solids 258 (1999) 11–19.

[68] S. He, Z. Li, E.-H. Yang, Quantitative characterization of anisotropic properties of the interfacial transition zone (ITZ) between microfiber and cement paste, Cem. Concr. Res. 122 (2019) 136–146.

[69] A. Fernández-Jiménez, A. Palomo, Mid-infrared spectroscopic studies of alkali-activated fly ash structure, Microporous Mesoporous Mater. 86 (2005) 207–214.

[70] I. Lecomte, C. Henrist, M. Liegeois, F. Maseri, A. Rulmont, R. Cloots, (Micro)-structural comparison between geopolymers, alkali-activated slag cement and Portland cement, J. Eur. Ceram. Soc. 26 (2006) 3789–3797.

[71] X. Yang, P. Roonasi, A. Holmgren, A study of sodium silicate in aqueous solution and sorbed by synthetic magnetite using in situ ATR-FTIR spectroscopy, J. Colloid Interface Sci. 328 (2008) 41–47.

[72] J.L. Provis, P. Duxson, G.C. Lukey, F. Separovic, W.M. Kriven, J.S. van Deventer, Modeling speciation in highly concentrated alkaline silicate solutions, Ind. Eng. Chem. Res. 44 (2005) 8899–8908.

[73] I. Garcia-Lodeiro, A. Fernández-Jiménez, D. Macphee, I. Sobrados, J. Sanz, A. Palomo, Stability of synthetic calcium silicate hydrate gels in presence of alkalis, aluminum, and soluble silica, Transp. Res. Rec. (2010) 52–57.

[74] J.F. Young, S. Mindess, D. Darwin, Concrete, Prentice Hall, 2002.

[75] L. Alarcon-Ruiz, G. Platret, E. Massieu, A. Ehrlacher, The use of thermal analysis in assessing the effect of temperature on a cement paste, Cem. Concr. Res. 35 (2005) 609–613.

[76] M.J. DeJong, F.-J. Ulm, The nanogranular behavior of CSH at elevated temperatures (up to 700 C), Cem. Concr. Res. 37 (2007) 1–12.

[77] E. Kapeluszna, Ł. Kotwica, A. Różycka, Ł. Gołek, Incorporation of Al in C-A-S-H gels with various Ca/Si and Al/Si ratio: microstructural and structural characteristics with DTA/TG, XRD, FTIR and TEM analysis, Constr. Build. Mater. 155 (2017) 643–653.

[78] M. Ben Haha, G. Le Saout, F. Winnefeld, B. Lothenbach, Influence of activator type on hydration kinetics, hydrate assemblage and microstructural development of alkali activated blast-furnace slags, Cem. Concr. Res. 41 (2011) 301–310.

[79] M.B. Haha, B. Lothenbach, G. Le Saout, F. Winnefeld, Influence of slag chemistry on the hydration of alkali-activated blast-furnace slag — part I: effect of MgO, Cem. Concr. Res. 41 (2011) 955–963.

[80] B. Lothenbach, P. Durdzinski, K. De Weerdt, Thermogravimetric Analysis, A Practical Guide to Microstructural Analysis of Cementitious Materials, CRC Press Oxford, UK, 2016, pp. 177–212.

[81] P. Rovnaník, P. Bayer, P. Rovnaníková, Characterization of alkali activated slag paste after exposure to high temperatures, Constr. Build. Mater. 47 (2013) 1479–1487.

[82] I.G. Richardson, Model structures for c-(a)-sh (i), Acta Crystallogr. Sect. B: Struct. Sci. Cryst. Eng. Mater. 70 (2014) 903–923.

[83] J.J. Chen, J.J. Thomas, H.F. Taylor, H.M. Jennings, Solubility and structure of calcium silicate hydrate, Cem. Concr. Res. 34 (2004) 1499–1519.

[84] R.J. Myers, S.A. Bernal, J.L. Provis, A thermodynamic model for C-(N-) ASH gel: CNASH_ss. Derivation and validation, Cem. Concr. Res. 66 (2014) 27–47.

[85] E. Ryshkewitch, Compression strength of porous sintered alumina and zirconia: 9th communication to ceramography, J. Am. Ceram. Soc. 36 (1953) 65–68.

[86] Z. Sun, G. Ye, S.P. Shah, Microstructure and early-age properties of Portland cement paste–effects of connectivity of solid phases, ACI Mater. J. 102 (2005) 122–129.

[87] B. Pichler, C. Hellmich, J. Eberhardsteiner, J. Wasserbauer, P. Termkhajornkit, R. Barbarulo, G. Chanvillard, Effect of gel–space ratio and microstructure on strength of hydrating cementitious materials: an engineering micromechanics approach, Cem. Concr. Res. 45 (2013) 55–68.

[88] A. Keulen, Q.L. Yu, S. Zhang, S. Grünewald, Effect of admixture on the pore structure refinement and enhanced performance of alkali-activated fly ash-slag concrete, Constr. Build. Mater. 162 (2018) 27–36.

[89] X. Gao, Q. Yu, H. Brouwers, Assessing the porosity and shrinkage of alkali activated slag-fly ash composites designed applying a packing model, Constr. Build. Mater. 119 (2016) 175–184.

[90] W. Kunther, S. Ferreiro, J. Skibsted, Influence of the Ca/Si ratio on the compressive strength of cementitious calcium–silicate–hydrate binders, J. Mater. Chem. A 5 (2017) 17401–17412.

[91] E. L'Hôpital, B. Lothenbach, K. Scrivener, D.A. Kulik, Alkali uptake in calcium alumina silicate hydrate (C-A-S-H), Cem. Concr. Res. 85 (2016) 122–136.

[92] F. Pelisser, P.J.P. Gleize, A. Mikowski, Effect of the Ca/Si molar ratio on the micro/nanomechanical properties of synthetic CSH measured by nanoindentation, J. Phys. Chem. C 116 (2012) 17219–17227.

[93] J.J. Beaudoin, L. Raki, R. Alizadeh, A 29Si MAS NMR study of modified C–S–H nanostructures, Cem. Concr. Compos. 31 (2009) 585–590.

[94] D. Hou, Y. Zhu, Y. Lu, Z. Li, Mechanical properties of calcium silicate hydrate (C–S–H) at nano-scale: a molecular dynamics study, Mater. Chem. Phys. 146 (2014) 503–511.

[95] C. Plassard, E. Lesniewska, I. Pochard, A. Nonat, Nanoscale experimental investigation of particle interactions at the origin of the cohesion of cement, Langmuir 21 (2005) 7263–7270.

[96] R.J.-M. Pellenq, H. Van Damme, Why does concrete set?: the nature of cohesion forces in hardened cement-based materials, MRS Bull. 29 (2004) 319–323.

[97] S. Lesko, E. Lesniewska, A. Nonat, J.-C. Mutin, J.-P. Goudonnet, Investigation by atomic force microscopy of forces at the origin of cement cohesion, Ultramicroscopy 86 (2001) 11–21.

[98] X. Ouyang, D. Koleva, G. Ye, K. Van Breugel, Understanding the adhesion mechanisms between CSH and fillers, Cem. Concr. Res. 100 (2017) 275–283.

[99] C. Labbez, I. Pochard, B. Jönsson, A. Nonat, C-S-H/solution interface: experimental and Monte Carlo studies, Cem. Concr. Res. 41 (2011) 161–168.

[100] C. Gunasekara, D.W. Law, S. Setunge, J.G. Sanjayan, Zeta potential, gel formation and compressive strength of low calcium fly ash geopolymers, Constr. Build. Mater. 95 (2015) 592–599.

[101] H.M. Jennings, Colloid model of C-S-H and implications to the problem of creep and shrinkage, Mater. Struct. 37 (2004) 59–70.

[102] R.J.M. Pellenq, N. Lequeux, H. van Damme, Engineering the bonding scheme in C–S–H: the iono-covalent framework, Cem. Concr. Res. 38 (2008) 159–174.